

Foregrounds for redshifted 21 cm studies of reionization: GMRT 153 MHz observations.

Sk. Saiyad Ali¹* Somnath Bharadwaj^{1†}, and Jayaram N. Chengalur ^{2‡}

¹ Department of Physics and Meteorology & Centre for Theoretical Studies, IIT Kharagpur, 721 302, India

² National Centre for Radio Astrophysics, TIFR, Post Bag 3, Ganeshkhind, Pune 411 007, India

2 February 2008

ABSTRACT

Foreground subtraction is the biggest challenge for future redshifted 21 cm observations to probe reionization. We use a short GMRT observation at 153 MHz to characterize the statistical properties of the background radiation across $\sim 1^\circ$ to sub-arcminutes angular scales, and across a frequency band of 5 MHz with 62.5 kHz resolution. The statistic we use is the visibility correlation function, or equivalently the angular power spectrum C_l . We present the results obtained from using relatively unsophisticated, conventional data calibration procedures. We find that even fairly simple minded calibration allows one to estimate the visibility correlation function at a given frequency $V_2(U, 0)$. From our observations we find that $V_2(U, 0)$ is consistent with foreground model predictions at all angular scales except the largest ones probed by our observations where the the model predictions are somewhat in excess. On the other hand the visibility correlation between different frequencies $\kappa(U, \Delta\nu)$, seems to be much more sensitive to calibration errors. We find a rapid decline in $\kappa(U, \Delta\nu)$, in contrast with the prediction of less than 1% variation across 2.5 MHz. In this case however, it seems likely that a substantial part of the discrepancy may be due to limitations of data reduction procedures.

Key words: cosmology: observations, cosmology: diffuse radiation, methods: statistical

1 INTRODUCTION

Observations of redshifted 21cm radiation from the large scale distribution of neutral hydrogen (HI) are perceived as one of the most promising future probes of the Universe at high redshifts (see Furlanetto, Oh & Briggs 2006 for a recent review). Observational evidence from quasar absorption spectra (Becker et al. 2001; Fan et al. 2002) and the CMBR (Spergel et al. 2007; Page et al. 2007) together imply that the HI was reionized over an extended period spanning the redshift range $6 \leq z \leq 15$ (for reviews see Barkana & Loeb 2001; Fan, Carilli & Keating 2006; Choudhury & Ferrara 2006). Determining how and when the Universe was reionized is one of the most important issues that will be addressed by future 21cm observations. The Giant Meter Wave Radio Telescope (GMRT¹; Swarup et al. 1991), currently functioning at several frequency bands in the range 150 to 1420 MHz is very well suited for carrying out initial

investigations towards detecting the reionization HI signal. There are several upcoming low-frequency instruments such as LOFAR², MWA³, 21CMA⁴ and SKA⁵ which are being built specifically with these observations in view.

It is currently perceived that a statistical analysis of the fluctuations in the redshifted 21 cm signal holds the greatest potential for observing HI at high redshifts (Bharadwaj and Sethi 2001; Zaldarriaga, Furlanetto & Hernquist 2004; Morales & Hewitt 2004; Bharadwaj and Ali 2005; Bharadwaj and Pandey 2005). Correlations among the visibilities measured in radio-interferometric observations directly probe the HI power spectrum at the epoch where the radiation originated. The reionization visibility signal at the GMRT is expected to be ~ 1 mJy and smaller (Bharadwaj and Ali 2005). This HI signal is present as a minute component of the background in all low frequency observations, and it is buried in foreground radiation from other astro-

* Email:saiyad@cts.iitkgp.ernet.in

† Email:somnath@cts.iitkgp.ernet.in

‡ Email:chengalu@ncra.tifr.res.in

¹ <http://www.gmrt.ncra.tifr.res.in>

² <http://www.lofar.org/>

³ <http://www.haystack.mit.edu/arrays/MWA>

⁴ <http://web.phys.cmu.edu/~past/>

⁵ <http://www.skatelescope.org/>

physical sources whose contribution is 4 to 5 orders of magnitude larger. Extracting the HI signal from the foregrounds is a major challenge.

Individual sources can be identified and removed from the image at a flux level which depends on the sensitivity. The contribution from the remaining discrete sources could be large enough to overwhelm the HI signal (Di Matteo et al. 2002). The diffuse synchrotron emission from our Galaxy (Shaver et al. 1999) is another important component. Foreground sources include free-free emission from ionizing halos (Oh & Mack 2003), faint radio loud quasars (Di Matteo et al. 2002) and synchrotron emission from low redshift galaxy clusters (DiMatteo. et al. 2004).

The foregrounds are expected to have a continuum spectra, and the contribution at two different frequencies separated by $\Delta\nu \sim 1$ MHz are expected to be highly correlated. The HI signal is expected to be uncorrelated at such a frequency separation and this holds the promise of allowing us to separate the signal from the foregrounds. A possible approach is to subtract a best fit continuum spectra for each line of sight (Wang et al. 2006) and then use the residuals to determine the HI power spectrum. An alternate approach is to first determine the statistical properties of the total radiation and then subtract out the smooth $\Delta\nu$ dependent part to extract the HI signal (Zaldarriaga, Furlanetto & Hernquist 2004). The issue of foreground removal has also been studied by Morales et al. (2006) and McQuinn et al. (2006).

It is crucial to accurately characterize the foregrounds in order to be able to detect the HI signal in future observations. In this paper we used GMRT observations to characterize the foregrounds at 153 MHz which corresponds to an HI signal from $z = 8.3$. To the best of our knowledge this is the first attempt to directly characterize the foregrounds at angular scales ($\sim 1^\circ$ to sub-arcminute) and frequency coverage (6 MHz with 62.5 kHz resolution) relevant for detecting the reionization HI signal.

We next present a brief outline of the paper. In Section 2 we describe the observations and data reduction while in Section 3 we present “visibility-correlations” which we use to quantify the statistical properties of our radio-interferometric data. Section 4 presents the predictions of existing foreground models, and in Section 5 we present our results and discuss their implications.

2 GMRT OBSERVATIONS AND DATA REDUCTION

The GMRT has a hybrid configuration (Swarup et al. 1991) where 14 of the 30 antennas are randomly distributed in a Central Square ~ 1.1 km \times 1.1 km in extent. These provide the uv coverage at small baselines. Here baseline refers to the antenna separation, and we use the two dimensional vector \mathbf{U} to denote the component perpendicular to the direction of observation. Note that \mathbf{U} has Cartesian components (u, v) and is dimensionless being in units of the observing wavelength. The shortest baseline at the GMRT is 100 m which comes down to around 60 m with projection effects. The rest of the antennas in the GMRT lie along three arms in an approximately ‘Y’ configuration. These provide uv coverage at long baselines (the longest baseline is 26 km). The diameter of each GMRT antenna is 45m. The hybrid configuration

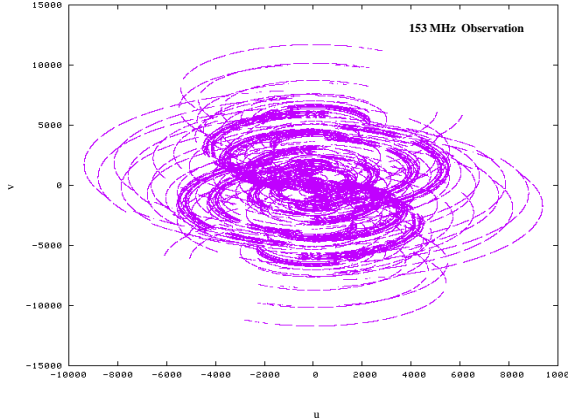


Figure 1. This shows the uv coverage of the GMRT data that we have analyzed. Here (u, v) are the antenna separations in wavelength units at the observing frequency 153 MHz.

gives reasonably good sensitivity for both compact and extended sources. Figure 1 shows the uv coverage of our GMRT observations.

On 15th June, 2005 we observed a field centered on Upsilon Andromedae (which is an extra-solar planetary system system at $\alpha_{2000} = 1^h 36^m 48^s$, $\delta_{2000} = 41^\circ 24' 23''$) for a total of 14 hours (including calibration). No emission that could be attributed to the planet was detected in our observations. The galactic co-ordinates are $l = 132.00^\circ$, $b = 20.67^\circ$. From the 408 MHz Haslam et al. (1982) map the sky temperature at this location is ~ 30 K (at 408 MHz), and there is no structure visible at the angular resolution of the map.

The observational set up used a total of 128 frequency channels spanning 8 MHz centered at 153 MHz. Each frequency channel is 62.5 kHz wide. A 6 MHz wide band-pass filter was introduced in the IF stage to exclude known strong Radio Frequency Interference (RFI), hence only 3/4 of the central channels contain astronomical signals. The integration time was 16 seconds, and visibilities were recorded for two orthogonal circular polarizations. The visibility data were analyzed using the Astronomical Image Processing Software (AIPS). The calibrator source 3C48 was used for flux, phase and bandpass calibration. The calibrator was observed every half hour so as to correct for temporal variations in the system gain. Standard AIPS tasks were used to flag all data that could be visually identified as being bad. We then made a high resolution image of the source using only a single channel (channel 35). The synthesized beam has a FWHM of $29'' \times 25''$ and the rms. noise in the CLEANed image is 9.5 mJy/Beam. All sources with flux density more than 30 mJy were fitted with clean components (CC), these components were merged and the visibilities corresponding to components with flux more than 8.6 mJy were subtracted from the multi-channel uv data using UVSUB. The value 8.6 mJy was chosen because we find predominantly positive clean components above this flux level whereas positive and negative components are equally abundant below this. The resultant uv data is now expected to be dominated by noise and residual RFI, since the majority of the point sources have been removed. Visually inspecting the data using the AIPS tasks VPLT and UVHGM, we decided to clip the data at 12 Jy whereby visibilities with

amplitude greater than 12 Jy were discarded. The clipping amplitude is in principle crucial since one would like to ensure that all baselines with RFI contributions have been discarded, without throwing away any good baselines. In practice we found that the exact clipping value does not make a substantial difference in our subsequent analysis. After this we added back the visibilities corresponding to all the CC components that we had subtracted. To first order, one could expect that at this stage all strong RFI has been removed.

The large field of view ($\theta_{\text{FWHM}} = 3.8^\circ$) of the GMRT at 150 MHz lead to considerable errors if the non-planar nature of the GMRT antenna distribution is not taken into account. We use the three dimensional (3D) imaging feature (e.g., Perley 1999) in the AIPS task IMAGR in which the entire field of view is divided into multiple subfields (facets) each of which is imaged separately. Here a $4^\circ \times 4^\circ$ field of view was imaged using 139 facets. We first collapsed 10 adjacent channels (channels 30 to 39) to make a single channel which was used to make a CLEANed image. This channel's frequency width 0.625 MHz (≤ 0.7 MHz) which is sufficiently small so as to avoid bandwidth smearing. The synthesized beam has $\text{FWHM} \sim 20''$ and the cleaned image has rms noise 4.6 mJy/Beam. The presence of a large number of sources in the field allows us to do self calibration loops to improve the image quality. The data went through 4 rounds of phase self calibration and a 5 th round where self calibration was done for both amplitude and phase. The time interval for the gain correction was chosen as 5, 5, 2, 2 and 2 minutes for the successive self calibration loops. The rms. noise in the final cleaned image was 3.1 mJy/Beam and the image quality had improved considerably. The final gain table was applied to all 128 frequency channels. Channels 21 to 100 of this data were then collapsed into 8 channels, each containing 10 of the original frequency channels. We use these to make a continuum image of the entire field. Some more data was flagged at this stage, and we then applied a final phase self calibration loop. This calibrated data was used to make the final cleaned image which is shown in Figure 2. The synthesized beam has a FWHM of $28'' \times 23''$, and an off-source RMS. noise level of 1.6 mJy/Beam. Note that several of the extended features like the one at $\alpha_{2000} = 01^h 41^m$, $\delta_{2000} = 40^\circ 24'$ are actually imaging artifacts around the brightest point sources. The brightest sources are also found to be accompanied by a region of negative flux density, these are presumably the results of residual phase errors which were not corrected for in our self calibration process. The maximum and minimum flux density in the final image are 820 mJy/Beam and -44 mJy/Beam respectively.

Recall that for this experiment, the sources visible in the final continuum image (Figure 2) are contaminants which have to be removed. Pixels with flux density above 8 mJy/Beam which were visually identified as sources and not imaging artifacts were fitted with clean components. The clean components were merged and the visibilities corresponding to these clean components were subtracted from the original full frequency resolution uv data using the AIPS task UVSUB. It is expected that at this stage most of the genuine sources in Figure 2 have been removed from the data. Figure 3 shows the final image made from the residual visibility data after UVSUB. The maximum and minimum flux density in this image are 25 mJy/Beam and -45 mJy/Beam respectively. The subsequent analysis was

done using the visibility data. We have analyzed the data both before and after the sources were subtracted, and we shall refer to these as **data I** (Initial - before source subtraction) and **data R** (residual - after source subtraction) respectively.

The final data contains 295868 baselines, each of which has visibilities for 2 circular polarizations and 96 frequency channels, of which we have used only the first 80 channels for the subsequent analysis. The visibilities from the two polarizations were combined for the subsequent analysis. The real and imaginary parts of the resulting visibilities have a mean value -0.56 mJy and 2.6 mJy respectively, and rms of 2.93 Jy for both in **data I**. For **data R** the real and imaginary parts of the visibilities have a mean -6.0 mJy and 1.1 mJy respectively whereas the rms is 2.42 Jy for both.

In the subsequent analysis it is often convenient to assume that the visibilities have a Gaussian distribution. Figure 4 shows the distribution of the real part of the visibilities for **data R**. We find that a Gaussian gives a reasonably good fit to the data within 2σ which contains the bulk of the data. The number counts predicted by the Gaussian falls much faster than the data at large visibility values $|Re(V)| > 6$ Jy. Deviation from Gaussian statistics is expected to mainly affect the error estimate on the visibility correlation. We expect this effect to be small, since only a small fraction of visibilities are discrepant. The imaginary part of **data R**, and the real and imaginary parts of **data I** all show a similar behaviour.

3 VISIBILITY CORRELATIONS

The visibility $V(\mathbf{U}, \nu)$ measured in a radio-interferometric observation is the sum of three different contributions

$$V(\mathbf{U}, \nu) = S(\mathbf{U}, \nu) + F(\mathbf{U}, \nu) + N(\mathbf{U}, \nu) \quad (1)$$

the HI signal $S(\mathbf{U}, \nu)$, astrophysical foregrounds $F(\mathbf{U}, \nu)$ and system noise $N(\mathbf{U}, \nu)$. We treat all three of these contributions as uncorrelated random variables with zero mean. The statistical properties of the visibility can be quantified through the two visibility correlation (henceforth the visibility correlation)

$$V_2(\mathbf{U}_1, \nu_1; \mathbf{U}_2, \nu_2) = \langle V(\mathbf{U}_1, \nu_1)V^*(\mathbf{U}_2, \nu_2) \rangle \quad (2)$$

and

$$V_2 = S_2 + F_2 + N_2 \quad (3)$$

where S_2 , F_2 and N_2 respectively refer to the signal, foreground and noise contributions to the visibility correlation.

The contribution from the HI signal S_2 is expected to be $\sim 10^{-7}$ Jy 2 or smaller at 150 MHz (Bharadwaj and Ali 2005). This is negligible compared to the expected foregrounds and noise contributions in our observations, and hence we ignore it in our further analysis.

The foreground contribution $F(\mathbf{U}, \nu)$ is the Fourier transform of the product of the foreground specific intensity distribution on the sky $I(\vec{\theta}, \nu)$ and the primary beam pattern of the individual GMRT antenna $A(\vec{\theta}, \nu)$. As mentioned earlier, this Fourier relation is strictly valid only if the field of view is small, and in this observation we expect considerable deviations at large baselines. As we are mainly

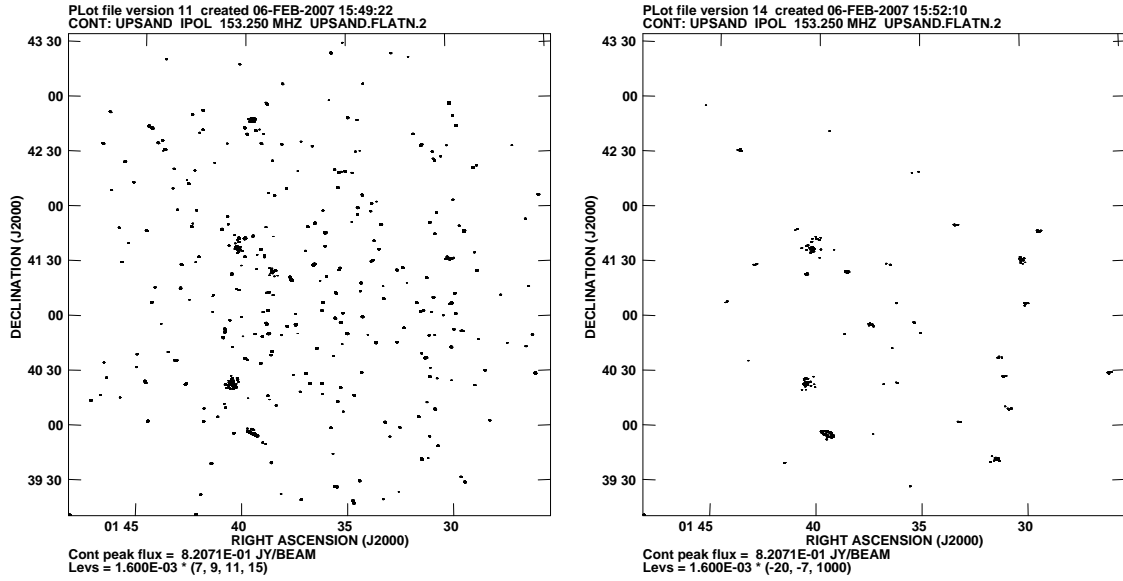


Figure 2. These shows our continuum image of bandwidth 5 MHz centered at 153 MHz. The $4^\circ \times 4^\circ$ field was imaged using 139 facets which have been combined using the AIPS task FLATN. The rms noise is 1.6mJy/Beam. The left and right panels shows positive and negative $7 - \sigma$ contours respectively. Note that many of the extended positive features and all negative features are imaging artifacts around the brightest sources.

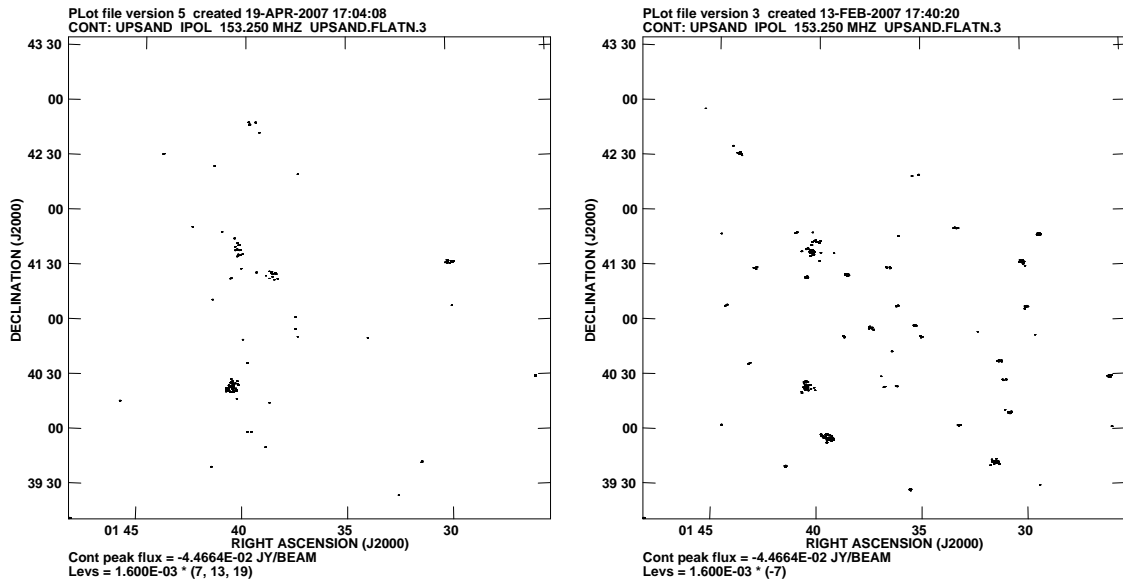


Figure 3. This is the same as the Figure 2 except that all the bright pixels > 8 mJy/Beam that were visually identified as being genuine sources and not artifacts have been fitted with clean components and removed from the visibility data from which this image was made. It is expected that most of the genuine sources have been removed from this data.

interested in the visibility correlations at small baselines, and also because the analysis is considerably more complicated otherwise, we assume the Fourier relation to hold. We can then express $F(\mathbf{U}, \nu)$ as a convolution

$$F(\mathbf{U}, \nu) = \int \tilde{I}(\mathbf{U}', \nu) \tilde{a}(\mathbf{U} - \mathbf{U}', \nu) d^2 \mathbf{U}'. \quad (4)$$

where $\tilde{I}(\mathbf{U}, \nu)$ and $\tilde{a}(\mathbf{U}, \nu)$ are the Fourier transform of $I(\vec{\theta}, \nu)$ and $A(\vec{\theta}, \nu)$ respectively. Assuming that the region of sky under observation is small so that it can be treated

as flat, we have

$$\langle \tilde{I}(\mathbf{U}_1, \nu_1) \tilde{I}(\mathbf{U}_2, \nu_2) \rangle = \delta_D^2(\mathbf{U}_1 - \mathbf{U}_2) \left(\frac{\partial B}{\partial T} \right)_{\nu_1} \left(\frac{\partial B}{\partial T} \right)_{\nu_2} \times C_{2\pi U_1}(\nu_1, \nu_2) \quad (5)$$

where $\delta_D^2(\mathbf{U}_1 - \mathbf{U}_2)$ is the two dimensional Dirac Delta function, $(\partial B / \partial T)_\nu = 2k_B \nu^2 / c^2$ is the conversion factor from brightness temperature to specific intensity and $C_l(\nu_1, \nu_2)$ is the multi-frequency angular power spectrum (MAPS; eg. Datta, Roy Choudhury, & Bharadwaj 2007) of the fore-

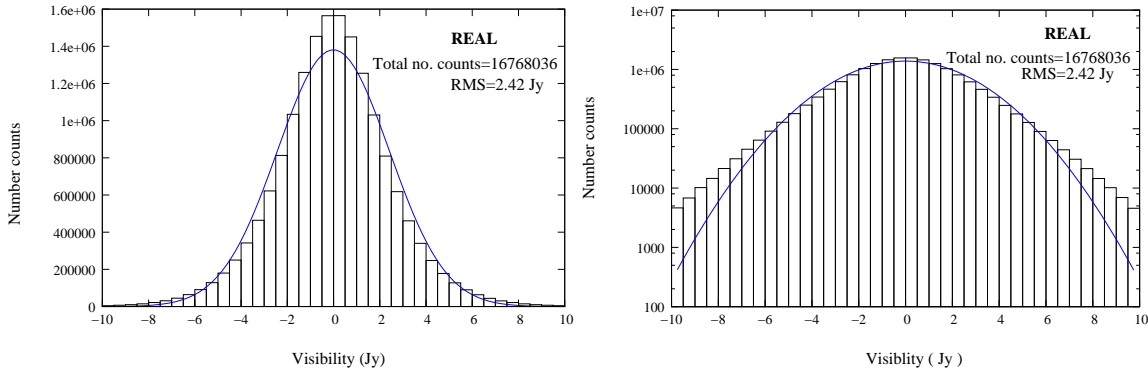


Figure 4. The distribution of visibilities after source subtraction (**data R**). The same plot is shown on a linear scale (left panel) and a log-linear scale (right panel). The data is plotted as a histogram, and a Gaussian with the corresponding mean and rms. (see text) is plotted as a solid line. The discrepancy at high amplitudes (≥ 6 Jy) is visible only in the right panel.

ground brightness temperature distribution. Using this to calculate the foreground contribution to the visibility correlation we have

$$F_2(\mathbf{U}_1, \nu_1; \mathbf{U}_2, \nu_2) = \int d^2U' \tilde{a}(\mathbf{U}_1 - \mathbf{U}', \nu_1) \tilde{a}^*(\mathbf{U}_2 - \mathbf{U}', \nu_2) \times \left(\frac{\partial B}{\partial T}\right)_{\nu_1} \left(\frac{\partial B}{\partial T}\right)_{\nu_2} C_{2\pi U'}(\nu_1, \nu_2). \quad (6)$$

The GMRT primary beam is well parametrized by a Gaussian $A(\vec{\theta}, \nu) = e^{-\theta^2/\theta_0^2}$ where $\theta_0 \approx 0.6 \times \theta_{\text{FWHM}} = 2.3^\circ$. There is a small variation in θ_0 ($\propto \nu^{-1}$) across the frequency band. Ignoring this ν dependence have $\tilde{a}(\mathbf{U}, \nu) = \tilde{a}(\mathbf{U}) = \pi\theta_0^2 \exp[-\theta_0^2\pi^2U^2]$. The integral in eq. (6) has a very small value unless the terms $\tilde{a}(\mathbf{U}_1 - \mathbf{U}')$ and $\tilde{a}^*(\mathbf{U}_2 - \mathbf{U}')$ have a considerable overlap *ie.* $|\mathbf{U}_1 - \mathbf{U}_2| < (\pi\theta_0)^{-1}$. This tells us that $F_2(\mathbf{U}, \nu_1; \mathbf{U} + \Delta\mathbf{U}, \nu_2)$ has a significant value only if $|\Delta\mathbf{U}| < (\pi\theta_0)^{-1}$ and is negligible otherwise. Further, $|\Delta\mathbf{U}| \ll U$ at the baselines of interest, and we may approximate $a^*(\mathbf{U} + \Delta\mathbf{U} - \mathbf{U}') \approx a^*(\mathbf{U} - \mathbf{U}')$ in eq. (6) and write

$$F_2(\mathbf{U}, \nu; \mathbf{U} + \Delta\mathbf{U}, \nu + \Delta\nu) = \left(\frac{\partial B}{\partial T}\right)_\nu^2 \int d^2U' |\tilde{a}(\mathbf{U} - \mathbf{U}')|^2 \times C_{2\pi U'}(\nu, \nu + \Delta\nu). \quad (7)$$

where we have ignored the $\Delta\nu$ dependence of θ_0 and $(\frac{\partial B}{\partial T})$.

The explicit reference to $\Delta\mathbf{U}$ can be dropped as it does not appear in the integral. We also assume that $C_{2\pi U}(\nu_1, \nu_2)$ is a slowly varying function of U as compared to $|\tilde{a}(\mathbf{U})|^2$ whereby $|\tilde{a}(\mathbf{U} - \mathbf{U}')|^2 \approx (\pi\theta_0^2/2)\delta_D^2(\mathbf{U} - \mathbf{U}')$ which gives

$$F_2(\mathbf{U}, \Delta\nu) = \frac{\pi\theta_0^2}{2} \left(\frac{\partial B}{\partial T}\right)^2 C_{2\pi U}(\Delta\nu) Q(\Delta\nu) \quad (8)$$

where $Q(\Delta\nu)$ incorporates the effect of the $\Delta\nu$ dependence of θ_0 and $(\frac{\partial B}{\partial T})$. We are mainly interested in the $\Delta\nu$ dependence, and we do not show the ν dependence explicitly. Equation (8) relates the angular power spectrum of the foreground contribution to the visibility correlations which can be determined from our observations.

The system noise makes a contribution

$$N_2(\mathbf{U}_1, \nu_1; \mathbf{U}_2, \nu_2) = \delta_{\mathbf{U}_1, \mathbf{U}_2} \delta_{\nu_1, \nu_2} \langle N^2 \rangle \quad (9)$$

which is non-zero only when a particular visibility is correlated with itself. For a single polarization, the rms. noise in the real part (or equivalently the imaginary part) of a

visibility is expected to be (Thompson, Moran & Swenson 1986)

$$\sigma = \frac{\sqrt{2}k_B T_{sys}}{A_{eff} \sqrt{\Delta\nu \Delta t}} \quad (10)$$

where T_{sys} is the total system temperature, k_B is the Boltzmann constant, A_{eff} is the effective collecting area of each antenna, $\Delta\nu$ is the channel width and Δt is correlator integration time. For the GMRT parameters⁶ this is predicted to be $\sigma = 1.03$ Jy for a single polarization. We have combined both polarizations, and so the variance in each visibility of the final data that we have analyzed is $2\sigma^2$. In eq. (9) the variance of the real and imaginary parts of the noise in a visibility contribute in quadrature and we have $\langle N^2 \rangle = 4\sigma^2$.

3.1 Estimating the visibility correlation.

We use the estimator

$$\hat{V}_2(U, \Delta\nu) = \overline{V(\mathbf{U}, \nu_i)V^*(\mathbf{U} + \Delta\mathbf{U}, \nu_i + \Delta\nu)} \quad (11)$$

where the bar denotes an average over the data under the assumptions

(i) The \mathbf{U} dependence is isotropic *ie.* V_2 depends only on the magnitude U and not the direction of \mathbf{U}

(ii) The $\Delta\nu$ dependence is the same if the frequency origin ν_i is shifted to another channel ν_j in the observation frequency band.

(iii) Only visibilities $V(\mathbf{U} + \Delta\mathbf{U}, \nu_i + \Delta\nu)$ at baselines $\mathbf{U} + \Delta\mathbf{U}$ within a disk of radius $|\Delta\mathbf{U}| \leq D < (\pi\theta_0)^{-1}$ centered at \mathbf{U} are correlated with $V(\mathbf{U}, \nu_i)$, and \hat{V}_2 is averaged over this disk.

Note that the second assumption above implies that $\hat{V}_2(U, \Delta\nu)$ gives an estimate of the average $\Delta\nu$ dependence across the entire frequency band. It also implies an average over positive and negative $\Delta\nu$ values. Besides this, the estimator is averaged over bins in U ($U_1 - U_2, U_2 - U_3, \dots$) so that we have $\hat{V}_2(U_i, \Delta\nu)$ at a few values U_i corresponding to the average baseline of the bins.

⁶ <http://www.gmrt.ncra.tifr.res.in>

The correlation of a visibility with itself introduces a noise contribution in the expectation value of this estimator. The noise contribution can be avoided (eg. Begum, Chengalur & Bharadwaj 2006) by excluding self-correlations *ie.* the visibility $V(\mathbf{U}, \nu_i)$ is correlated with every baseline $V(\mathbf{U} + \Delta\mathbf{U}, \nu_i + \Delta\nu)$ within a disk $|\Delta\mathbf{U}| < D$ except itself. The expectation value of the estimator has a value

$$\langle \hat{V}_2(U, \Delta\nu) \rangle = F_2(U, \Delta\nu). \quad (12)$$

which provides an unbiased estimate of the foregrounds. The system noise makes a contribution only to the uncertainty or the error in the estimator. The expectation value of the estimator is real. The value of the estimator determined from an observation will, in general, have a real and an imaginary part. The real part contains the foreground information, whereas the imaginary part of the observed value of the estimator can be attributed to statistical fluctuations in the foregrounds and the noise.

3.2 Error Estimates

The expected uncertainty or statistical fluctuations in the real part of the estimator

$$\sqrt{\langle (\Delta\hat{V}_2)^2 \rangle} \equiv \sqrt{\langle (\hat{V}_2 - \langle \hat{V}_2 \rangle)^2 \rangle} \quad (13)$$

is the sum of two contributions

$$\langle (\Delta\hat{V}_2)^2 \rangle = (\Delta F_2)^2 + (\Delta N_2)^2. \quad (14)$$

If we assume that the foregrounds are a Gaussian random field, the foreground contribution to the error is

$$[\Delta F_2(U_i, \Delta\nu)]^2 = \frac{1}{N_E} \left[\frac{F_2(U_i, 0) + F_2(U_i, \Delta\nu)}{2} \right] \quad (15)$$

where N_E is the number of independent estimates of $F_2(U, \Delta\nu)$ that contribute to $\hat{V}_2(U_i, \Delta\nu)$. The baselines within a disk of radius $\sim (\pi\theta_0)^{-1}$ in uv space (Figure 1) are correlated, and all the baselines within such a disk provide only one independent estimate of the visibility correlation. For each U bin N_E is determined by counting the number of such regions with the uv coverage of our observations.

The system noise contribution in any two visibilities are uncorrelated, and hence

$$[\Delta N_2(U, \Delta\nu)]^2 = \frac{\langle N^2 \rangle^2}{2N_P} = \frac{8\sigma^4}{N_P} \quad (16)$$

where N_P is the number of visibility pairs that contribute to the estimator $\hat{V}_2(U, \Delta\nu)$ for a particular U bin and $\Delta\nu$ separation.

The error in the imaginary part of the estimator also is a sum of two contributions. The foreground contribution is somewhat different from eq. (15) and we have

$$[\Delta F_2(U_i, \Delta\nu)]^2 = \frac{1}{N_E} \left[\frac{F_2(U_i, 0) - F_2(U_i, \Delta\nu)}{2} \right] \quad (17)$$

while the system noise contribution is the same as eq. (16).

4 FOREGROUND MODEL PREDICTIONS

We consider only the two most dominant foreground components namely extragalactic radio sources and the diffuse

synchrotron radiation from our own Galaxy. The free-free emissions from our Galaxy and external galaxies is around 1% of the total foreground contribution (Shaver et al. 1999), and we ignore this in our analysis. For each foreground component the MAPS can be modeled as

$$C_l(\nu_1, \nu_2) = A \left(\frac{\nu_f}{\nu_1} \right)^{\bar{\alpha}} \left(\frac{\nu_f}{\nu_2} \right)^{\bar{\alpha}} \left(\frac{1000}{l} \right)^{\beta} I_l(\nu_1, \nu_2) \quad (18)$$

where $\nu_f = 130$ MHz, and for each foreground component A , β and $\bar{\alpha}$ are the amplitude, the power law index of the angular power spectrum and the mean spectral index respectively. The actual spectral index varies with line of sight across the sky and this causes the foreground contribution to decorrelate with increasing frequency separation $\Delta\nu = |\nu_2 - \nu_1|$ which is quantified through the foreground frequency decorrelation function $I_l(\nu_1 \nu_2)$ (Zaldarriaga, Furlanetto & Hernquist 2004) which has been modeled as

$$I_l(\nu_1, \nu_2) = \exp \left[-\log_{10}^2 \left(\frac{\nu_2}{\nu_1} \right) / 2\xi^2 \right]. \quad (19)$$

The model parameters values that we have used are discussed below and are given in Table 1.

Resolved extragalactic radio sources (point sources) dominate the radio sky at 150 MHz. Di Matteo et al. (2002) have used the 6C survey (Hales, Baldwin & Warner 1988), and the 3CR survey and the 3 CRR catalogue (Laing, Riley & Longair 1983) to estimate this contribution. The limiting flux density of these surveys was ~ 100 mJy and the extrapolation to fainter sources is rather uncertain. Di Matteo et al. (2002) have fitted the differential source counts using a double power-law with the change in slope occurring at 880 mJy. Since the brightest source in our image has a flux density below 880 mJy we use only the fit to the fainter part

$$\frac{dN}{dS} = \frac{4000}{Jy \cdot Sr} \cdot \left(\frac{S}{1Jy} \right)^{-1.75}. \quad (20)$$

These sources make two distinct contributions to MAPS, the first being the Poisson noise arising from the discrete nature of these sources and the second arising from the clustering of the sources. Table 1 shows the respective parameters based on the estimates of Di Matteo et al. (2002) who assume that these sources are clustered like galaxies today or as Lyman-break galaxies (Giavalisco et al. 1998) at $z \sim 3$. Using these in eq. (8) to calculate the foreground contribution to the visibility correlation at 153 MHz for $\Delta\nu = 0$, we have the Poisson term

$$F_2(U, 0) = 7.6 \left(\frac{S_c}{Jy} \right)^{1.25} Jy^2, \quad (21)$$

and the clustering term

$$F_2(U, 0) = 0.51 \left(\frac{S_c}{Jy} \right)^{0.5} \left(\frac{U}{1000} \right)^{-1.1} Jy^2. \quad (22)$$

Here it is assumed that sources with flux greater than S_c have been identified from continuum images and removed from the data. The brightest source in our initial image has $S \sim 890$ mJy and we use this value for S_c when comparing model predictions with results from **data I**. For **data R** we have used $S_c = 8$ mJy as we have used this as the limiting value for our source subtraction (Section 2).

Table 1. Fiducial values of the parameters used for characterizing different foreground contributions

Foregrounds	$A(\text{mK}^2)$	$\bar{\alpha}$	β	ξ
Point source (Poisson part)	$1.2 \times 10^4 \left(\frac{S_{\text{cut}}}{\text{Jy}}\right)^{1.25}$	2.07	0	1
Point source (clustered part)	$6.1 \times 10^3 \left(\frac{S_{\text{cut}}}{\text{Jy}}\right)^{0.5}$	2.07	1.1	2
Galactic synchrotron	700	2.80	2.4	4

The uncertainty or error in the model prediction for these radio sources is also a sum of two parts. The error in the clustering part can be estimated using eq. (15). For the Poisson part the variance of F_2 involves the fourth moment of the differential source count and we have

$$[\Delta F_2(U, 0)]^2 = \left(\frac{s_c}{\text{Jy}}\right)^{2.5} \left[63.2 - 1.54 \left(\frac{s_c}{\text{Jy}}\right)^{0.75} \right]. \quad (23)$$

The diffuse Galactic synchrotron radiation is believed to be produced by cosmic ray electrons propagating in the magnetic field of the Galaxy (Ginzburg & Syrovatskii 1969). This has an angular power spectrum that scales as $C_l \sim l^{-2.4}$ (Tegmark et al. 2000), though this slope (β) is rather uncertain. The analysis of radio surveys at 408 MHz, 1.42 GHz, and 2.326 GHz (Haslam et al. 1982; Reich 1982; Reich & Reich 1988; Jonas, Baart, & Nicolson 1998) show the spectral index to be $\bar{\alpha} \approx 2.8$ which is in general agreement with result of Platania et al. (1998). For the synchrotron radiation, in Table 1 we have adopted the parameters from Santos et al. (2005) which gives

$$F_2(U, 0) = 4.2 \times 10^{-3} \left(\frac{U}{1000}\right)^{-2.4} \text{Jy}^2. \quad (24)$$

We note that the amplitude of the synchrotron contribution is very sensitive to the spectral index whose value is quite uncertain. The value is in the range $2.5 \leq \bar{\alpha} \leq 3$, and the amplitude increases by nearly an order of magnitude if $\bar{\alpha} = 3$ instead of $\bar{\alpha} = 2.8$ as assumed here.

The error for the synchrotron prediction can be calculated using eq. 15. The total error in the model predictions is calculated by adding the variances from the different contributions.

For the frequency separations of our interest ($\Delta\nu < 2.5$ MHz), for all the foreground components the $(\nu_2/\nu_f)^{\bar{\alpha}}$ term in equation (18) introduces a larger $\Delta\nu$ dependence in $C_l(\Delta\nu)$ as compared to the frequency decorrelation function $I(\nu_1, \nu_2)$. When calculating $F_2(U, \Delta\nu)$ it is necessary to also incorporate $Q(\Delta\nu)$ (eq. 8) which has the $\Delta\nu$ dependence arising from θ_0 and $(\partial B/\partial T)_\nu$. All of these predict a smooth $\Delta\nu$ dependence, and we may use a Taylor series expansion

$$F_2(U, \Delta\nu) = F_2(U, 0) \left[1 + B \left(\frac{\Delta\nu}{\nu}\right)^2 \dots \right] \quad (25)$$

where B is a constant of order unity. The $\Delta\nu/\nu$ term does not appear in eq. (25). This term cancels out because the

estimator $\hat{V}_2(U, \Delta\nu)$ averages positive and negative $\Delta\nu$ values. We use $B = 1$ to make an order of magnitude estimate. The expected change in $F_2(U, \Delta\nu)$ is $\sim 3 \times 10^{-2}\%$ for $\Delta\nu = 2.5$ MHz. The key point here is that $F_2(U, \Delta\nu)$ is predicted to change very slowly with $\Delta\nu$, and the change is also very small.

5 RESULTS AND DISCUSSION

We have determined the observed value $V_2(U, \Delta\nu)$ of the visibility correlation estimator $\hat{V}_2(U, \Delta\nu)$ for **data I** and **data R** which are before and after source subtraction respectively. Baselines in the range $20 \leq U \leq 2 \times 10^4$, and frequency channels 21 to 100 were used for the analysis. Visibilities $V(\mathbf{U} + \Delta\mathbf{U}, \nu + \Delta\nu)$ within the disk $|\Delta\mathbf{U}| \leq D = 5$ were correlated with $V(\mathbf{U}, \nu)$. Here $\Delta\nu$ was restricted to $|\Delta\nu| < 2.5$ MHz which corresponds to a separation of 40 channels. Note that the correlation of a visibility with itself was not included. The value of D was chosen such that it is both less than $(\pi\theta_0)^{-1} = 8$, and also large enough that a reasonable number of visibility pairs that contribute to the correlation. Figure 5 shows $V_2(U, \Delta\nu)$ as a function of U for $\Delta\nu = 0$. Equivalently, we may also interpret this as the multi-frequency angular power spectrum $C_l(\Delta\nu)$ at $\Delta\nu = 0$.

For both the data-sets the real part of $V_2(U, 0)$ is found to be considerably larger than the imaginary part. This is consistent with the discussion of Section 3.1, and we expect the real part to provide an estimate of the foreground contribution $V_2(U, 0)$. The $1-\sigma$ error bars shown in the figure have been determined based on the error estimates discussed in Section 3.2. The uncertainty in $F_2(U, 0)$ is mainly due to the limited number of independent estimates, the system noise makes a smaller contribution. Though the results for **data I** over the range $200 \leq U \leq 2 \times 10^4$ looks like a power law $V_2(U, 0) \propto U^{-\alpha}$ with a very small slope $0 \leq \alpha \leq 0.25$, we do not find a fit with an acceptable value of χ^2 per degree of freedom.

The real part of $V_2(U, 0)$ falls to nearly one-fourth of its original value at most of the U bins when the directly detected sources are subtracted out. This indicates that a large part of the contribution to $V_2(U, 0)$ in **data I** is from these resolved sources, and we may interpret $V_2(U, 0)$ as arising primarily from these sources. **Data R** is expected to contain contributions from point sources below the detection limit of our image, diffuse sources, system noise, limitations in our imaging and source subtraction procedure and residual RFI. We will assume for the moment that these effects can be ignored, but return to this issue later in this section.

Figure 6 shows the observed $V_2(U, 0)$ plotted against the predictions of the foreground models discussed in Section 4. The brightest source in our image has flux 890 mJy. Based on this we use $S_c = 900$ mJy for the point source contribution to **data I**. The clustering of point sources dominates at baselines $U < 150$ ($\theta > 0.7^\circ$), while the Poisson fluctuations of the point sources dominates at larger baselines. The diffuse Galactic synchrotron radiation is much smaller than the point source contribution at all baselines. The errors in the model prediction are quite large and are mainly due to the Poisson fluctuations of the point sources. The model predictions are found to be consistent with the observed values of $V_2(U, 0)$ except at the smallest U value which cor-

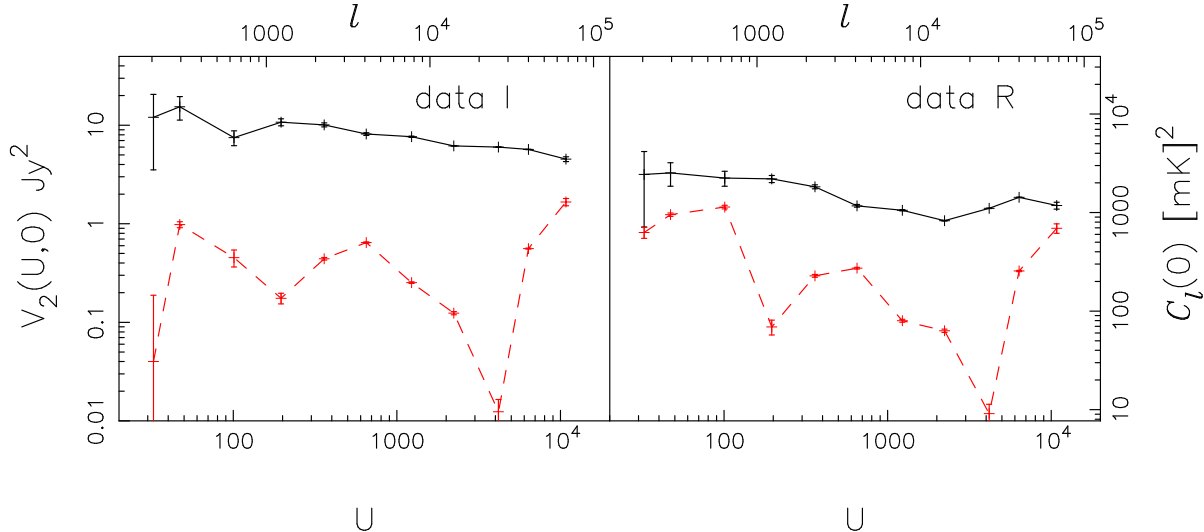


Figure 5. This shows the real (upper curve) and imaginary (lower curve) parts of the observed visibility correlation $V_2(U, 0)$ as a function of U for the two data-sets indicated in the figure. As shown here, this may also be interpreted as $C_l(0)$ as a function of l .

responds to an angular scale of $\sim 1.8^\circ$. At these baselines the convolution with the primary beam pattern (eq. (6)) becomes important. We have not included this, and the actual model predictions would possibly be somewhat smaller if this were included. As noted in Section 4., the amplitude of the synchrotron contribution is very sensitive to the value of the spectral index. The amplitude decreases by a factor of ~ 18 if $\bar{\alpha} = 2.5$ instead of the value $\bar{\alpha} = 2.8$ used here. This changes the total foreground contribution only at small baselines ($U \leq 100$) where the model then becomes consistent with our observations.

The limiting flux for source subtraction is ~ 8 mJy, and hence we use $S_c = 10$ mJy for **data R**. The model prediction is dominated by Galactic synchrotron radiation at $U < 150$, point source clustering in the range $150 \leq U \leq 2 \times 10^3$ and point source Poisson fluctuations at $U > 2 \times 10^3$. The model predictions fall short of the observations at all baselines except the smallest U value where it overshoots the observations. Since the model prediction for $S_c = 10$ mJy falls very much short of the observations, we also consider $S_c = 100$ mJy where the dominant contribution is Galactic synchrotron at $U < 60$, point source clustering in the range $60 \leq U \leq 400$ and point source Poisson fluctuations at $U > 400$. We find that the observations are slightly above the $1 - \sigma$ error-bars at baselines $U > 100$, whereas they exceed the model predictions at baselines $U < 100$. A point to note is that at the smallest baseline the prediction for the Galactic synchrotron radiation exceeds the observation. This may be a consequence of the possibility that the background radiation is relatively low in the direction of our observation. Estimates from the Haslam et al. (1982) map at 408 MHz show a relatively low brightness temperature of ~ 30 K towards the direction of our observation.

We quantify the $\Delta\nu$ dependence of $V_2(U, \Delta\nu)$ using $\kappa(U, \Delta\nu)$ which is defined as

$$\kappa(U, \Delta\nu) = \frac{V_2(U, \Delta\nu)}{V_2(U, 0)}. \quad (26)$$

We expect the visibilities $V(\mathbf{U}, \nu)$ and $V(\mathbf{U}, \nu + \Delta\nu)$ to get decorrelated as $\Delta\nu$ is increased, and hence we expect

$0 \leq |\kappa(U, \Delta\nu)| \leq 1$. Figure 7 shows $\kappa(U, \Delta\nu)$ for different values of U . The foreground models predict a smooth $\Delta\nu$ dependence for $\kappa(U, \Delta\nu)$. The departure from $\kappa(U, \Delta\nu) = 1$ is predicted to be less than 1% for $\Delta\nu < 2.5$ MHz. The observed behavior of $\kappa(U, \Delta\nu)$ is quite different from the model predictions. At the small baselines $U < 1000$ we find that $\kappa(U, \Delta\nu)$ falls sharply within the first three channels. In the $U = 47$ bin $\kappa(U, \Delta\nu)$ fluctuates at large $\Delta\nu$ whereas it remains roughly constant at $U = 360$. In both cases this value of $\kappa(U, \Delta\nu)$ is smaller for **data R** as compared to **data I**. At $U = 2200$, for **data I** $\kappa(U, \Delta\nu)$ falls gradually with increasing $\Delta\nu$, and the visibilities are uncorrelated ($\kappa(U, \Delta\nu) \sim 0$) by $\Delta\nu \sim 2.5$ MHz. Interestingly, for **data R** we find that $\kappa(U, \Delta\nu)$ shows a sudden increase to $\kappa(U, \Delta\nu) > 1$ at very small $\Delta\nu$ (< 0.5 MHz), after which $\kappa(U, \Delta\nu)$ falls and becomes negative by $\Delta\nu \sim 2$ MHz. It appears that in this U bin our source subtraction procedure has introduced excess correlations between the visibilities at small $\Delta\nu$ and introduces anti correlations at large $\Delta\nu$. At $U = 4200$, for **data I** the value of $\kappa(U, \Delta\nu)$ oscillates with increasing $\Delta\nu$. At large $\Delta\nu$ **data R** also shows a similar behavior except that the $\kappa(U, \Delta\nu)$ values are smaller. The behavior of **data R** is quite different from that of **data I** at very small $\Delta\nu$ where there are two small oscillations that cross $\kappa(U, \Delta\nu) = 1$.

The first point that emerges from our results is that the observed visibility correlations $V_2(U, 0)$ is consistent with the predictions of the existing foreground models at all baselines except the smallest one which probes angular scales $\sim 1^\circ$. The observations are in excess of the model prediction at the smallest baseline. The second point is that $V_2(U, \Delta\nu)$ shows considerable $\Delta\nu$ dependence, there being changes of order unity within $\Delta\nu = 2.5$ MHz. This rapid change in the visibilities $V_2(U, \nu)$ across frequency channels is contrary to the foreground models which predict changes less than 1%.

It is well appreciated that accurate subtraction of the foreground emission requires very exacting calibration. In contrast, we have followed fairly standard calibration procedures. As such it seems likely that the discrepancy between our observations and existing predictions is probably not

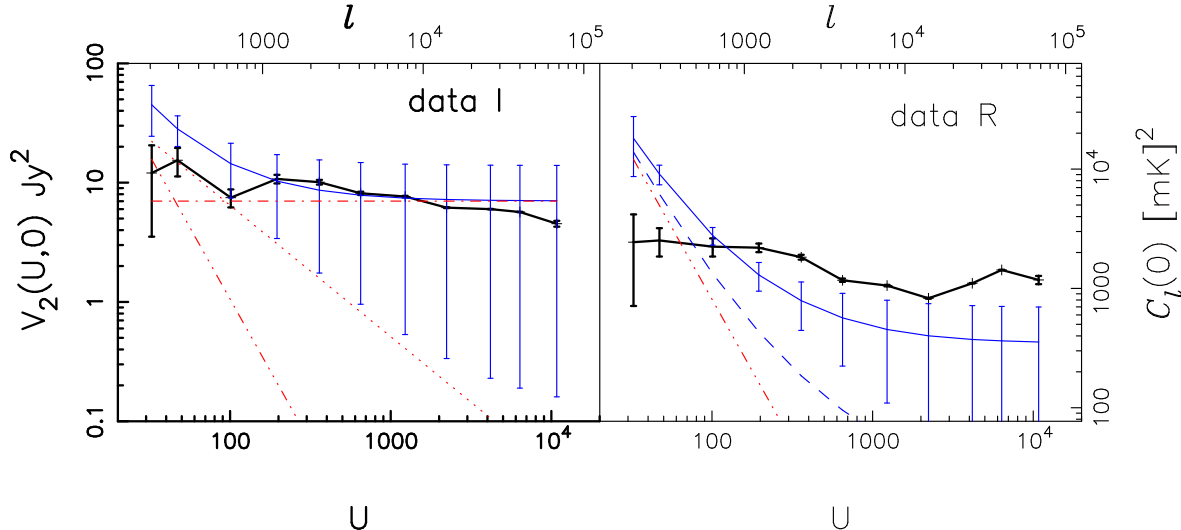


Figure 6. The thick solid line shows the real part of the observed visibility correlation $V_2(U,0)$ as a function of U for the two data-sets indicated in the figure. As shown here, this may also be interpreted as $C_l(0)$ as a function of l . For **data I** the thin solid line shows the total model prediction for $S_c = 900$ mJy. Also shown are the contributions from point source Poisson (dash-dot), point source clustering (dot) and Galactic synchrotron (dash-dot-dot-dot). For **data R** the thin solid line shows the total model predictions for $S_c = 100$ mJy and the long dashed line for 10 mJy. The dash-dot-dot-dot curve shows the Galactic synchrotron contribution.

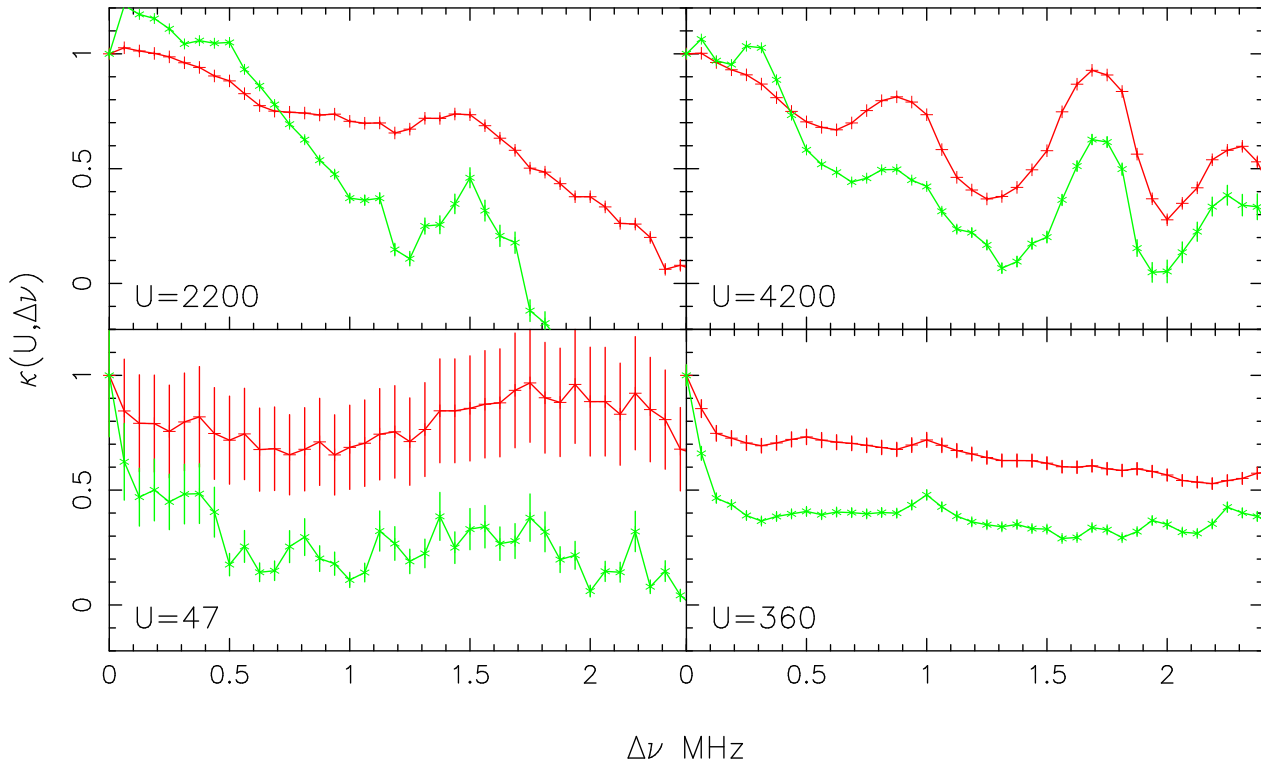


Figure 7. This shows $\kappa(U, \Delta\nu)$ as a function of $\Delta\nu$ for the different U values shown in the figure. The upper curve (at large $\Delta\nu$) shows **data I** while the lower shows **data R**.

genuine; indeed there are several purely instrument related possibilities that may account for the discrepancies between our observational findings and existing models for the foreground emission. We take up first the issue of calibration error which will introduce phase and amplitude errors in the visibilities. The fact that the values of $\kappa(U, \Delta\nu)$ are generally smaller for **data R** as compared to **data I** may be inter-

preted as indicating that the visibilities $V(U, \nu)$ are a combination of two parts, a correlated part which arises from for e.g. the effect of calibration errors on discrete sources, and another whose contribution to different channels is uncorrelated. The ‘halos’ that we see around the bright sources is a clear indication that calibration problems exist in our data. Phase errors which vary with channel would cause decorre-

lation of the visibilities across different frequencies. Further, one would expect that the phase errors increase with increasing baseline length, which is qualitatively consistent with what we see in Fig. 7. In contrast to the situation for $\kappa(U, \Delta\nu)$, the contribution from the source subtraction residuals to $V_2(U, 0)$ (Fig. 6) can be estimated to be small as follows. There are only ~ 100 imaging artifacts with absolute value of flux > 20 mJy (**Data R**, Figure 3), while about 10,000 such sources would be needed to produce the observed visibility correlation of ~ 4 Jy² (**Data R**, Figure 6).

The 2D Fourier relation between the sky brightness and the visibilities assumed in Section 3 is not strictly valid for GMRT's large field of view ($\theta_{\text{FWHM}} = 3.8^\circ$). In addition to $u - v$ which are the components of the baseline in the plane normal to the direction of observation, it is also necessary to consider w the component along the observing direction. This is a possible source of error in our visibility correlation analysis. To assess the impact of the w term we have repeated the analysis using only a limited range of baselines for which $w \leq 100$. We find that limiting the maximum w value does not make any qualitative change in our results. The conclusions are unchanged even if we impose $w \leq 50$.

Residual RFI is another possibility. The visibilities were clipped at 12 Jy (Section 2.) and this is expected to remove the strong RFI, but weak RFI contributions will persist in the data. The RFI electric fields at any two antennas are correlated with a time delay τ which depends on position of the RFI source relative to the antennas and the direction of observation. The RFI contribution behaves like the system noise if τ is greater than τ_c the coherence time of the RFI signal. In this case the RFI effectively increases σ the rms. fluctuations of the visibilities. This only changes the error estimates, and does not affect the expected visibility correlations. RFI sources for which $\tau < \tau_c$ are expected to affect the visibility correlations. This contribution will depend on the distribution of the time delays τ_s and the frequency spectrum of the RFI sources. The analysis of this is beyond the scope of this paper. Work is currently underway at the GMRT to implement more sophisticated real time as well as offline RFI mitigation schemes. Future observations will help assess the improvement that these schemes as well as better calibration procedures make on the problem of foreground subtraction. Polarization leakage is another important issue that we plan to take up in future work.

6 ACKNOWLEDGMENT

SSA and SB would like to thank Prasun Dutta and Kanan K. Datta for their help. The data used in this paper were obtained using GMRT. The GMRT is run by the National Centre for Radio Astrophysics of the Tata Institute of Fundamental Research. We thank the GMRT staff for making these observations possible.

REFERENCES

Barkan, R. and Loeb, A. 2001, *Phys. Rep.*, 349, 125
 Becker, R.H., et al., 2001, *AJ*, 122, 2850
 Begum, A., Chengalur, J. N., & Bhardwaj, S. 2006, *MNRAS*, 372, L33
 Bharadwaj, S. & Sethi, S. 2001, *JApA*, 22, 293
 Bharadwaj, S. & Ali, S. S. 2005, *MNRAS*, 356, 1519
 Bharadwaj, S. & Pandey, S.K. 2005, *MNRAS*, 358, 968
 Choudhury, T. R., Ferrara, A., Preprint: astro-ph/0603149, 2006a
 Datta, K. K. Roy Choudhury, T., & Bharadwaj, S. 2007, *MNRAS*, 378, 119
 Di Matteo, T., Ciardi, B., & Miniati, F. 2004, *MNRAS*, 355, 1053
 Di Matteo, T., Perna, R., Abel, T. & Rees, M.J., 2002, *Ap.J*, 564, 576
 Fan, X., et al. 2002, *AJ*, 123, 1247
 Fan, X., Carilli, C.L. and Keating, B., 2006, *Ann. Rev. Astron. Astrophys.*, 44, 415
 Furlanetto, S. R., Oh, S. P., & Briggs, F., 2006, *Phys. Rept.* 433, 181
 Giavalisco, M., Steidel, C. C., Adelberger, K. L., Dickinson, M. E., Pettini, M., & Kellogg, M. 1998, *APJ*, 503, 543
 Ginzburg, V. L. & Syrovatskii, S. I., 1969, *Ann. Rev. Astron. Astrophys.*, 7, 375
 Hales, S. E. G., Baldwin, J. E., & Warner, P. J. 1988, *MNRAS*, 234, 919
 Haslam, C. G. T., Salter, C. J., Stoffel, H., Wilson, W. E., 1982, *A&AS*, 47, 1.
 Jonas, J.L., Baart, E.E., Nicolson, G.D., 1998, *MNRAS*, 297, 977
 Laing, R. A., Riley, J. M. & Longair, M. S. 1983, *MNRAS*, 204, 151
 McQuinn, M., Zahn, O., Zaldarriaga, M., Hernquist, L. & Furlanetto, S. R., 2006, *Ap.J*, 653, 815
 Morales, M. F. and Hewitt, J., 2004, *ApJ*, 615, 7
 Morales, M. F., Bowman, J. D. & Hewitt, J. N., 2006, *Ap.J*, 648, 767
 Oh, S.P., & Mack, K. J., 2003, *MNRAS*, 346, 871
 Page, L., et al. 2007, *ApJS*, 170, 335
 Perley, R.A. 1999, *ASP Conference Series*, "Synthesis Imaging in Radio Astronomy II", Eds. G. B. Taylor, C. L. Carilli, and R. A. Perley, Vol. 180, p.19
 Platania, P., Bensadoun, M., Bersanelli, M., de Amici, G., Kogut, A., Levin, S., Maino, D., & Smoot, G. F. 1998, *Ap.J*, 505, 473
 Reich, W., 1982, *A&AS*, 48, 219.
 Reich, P. & Reich, W., 1988, *A&AS*, 74, 7.
 Santos, M.G., Cooray, A. & Knox, L. 2005, 625, 575
 Shaver, P. A., Windhorst, R. A., Madau, P. & de Bruyn, A. G., 1999, *Astron. & Astrophys.*, 345, 380
 Spergel, D. N., et al. 2007, *ApJS*, 170, 377
 Swarup, G., Ananthakrishnan, S., Kapahi, V. K., Rao, A. P.,
 Tegmark, M., Eisenstein, D. J., Hu, W., de Oliveira-Costa, A., 2000, *Ap.J*, 530, 133.
 Thompson, A.R., Moran, J.M., & Swenson, G.W. 1986, *Interferometry and Synthesis in Radio Astronomy*, John Wiley & Sons, pp. 160
 Wang, X., Tegmark, M., Santos, M., & Knox, L., 2006, *ApJ*, 650, 529
 Zaldarriaga, M., Furlanetto, S. R., & Hernquist, L. 2004, *Ap.J*, 608, 622